Operando visualisation of dendrite growth and dissolution. Three-dimensional images of grown dendrites based on reconstruction of synchrotron x-ray tomography data. High-resolution and reconstructed three-dimensional images of the deposits inside the battery separator generated by Focused Ion Beam SEM tomography.

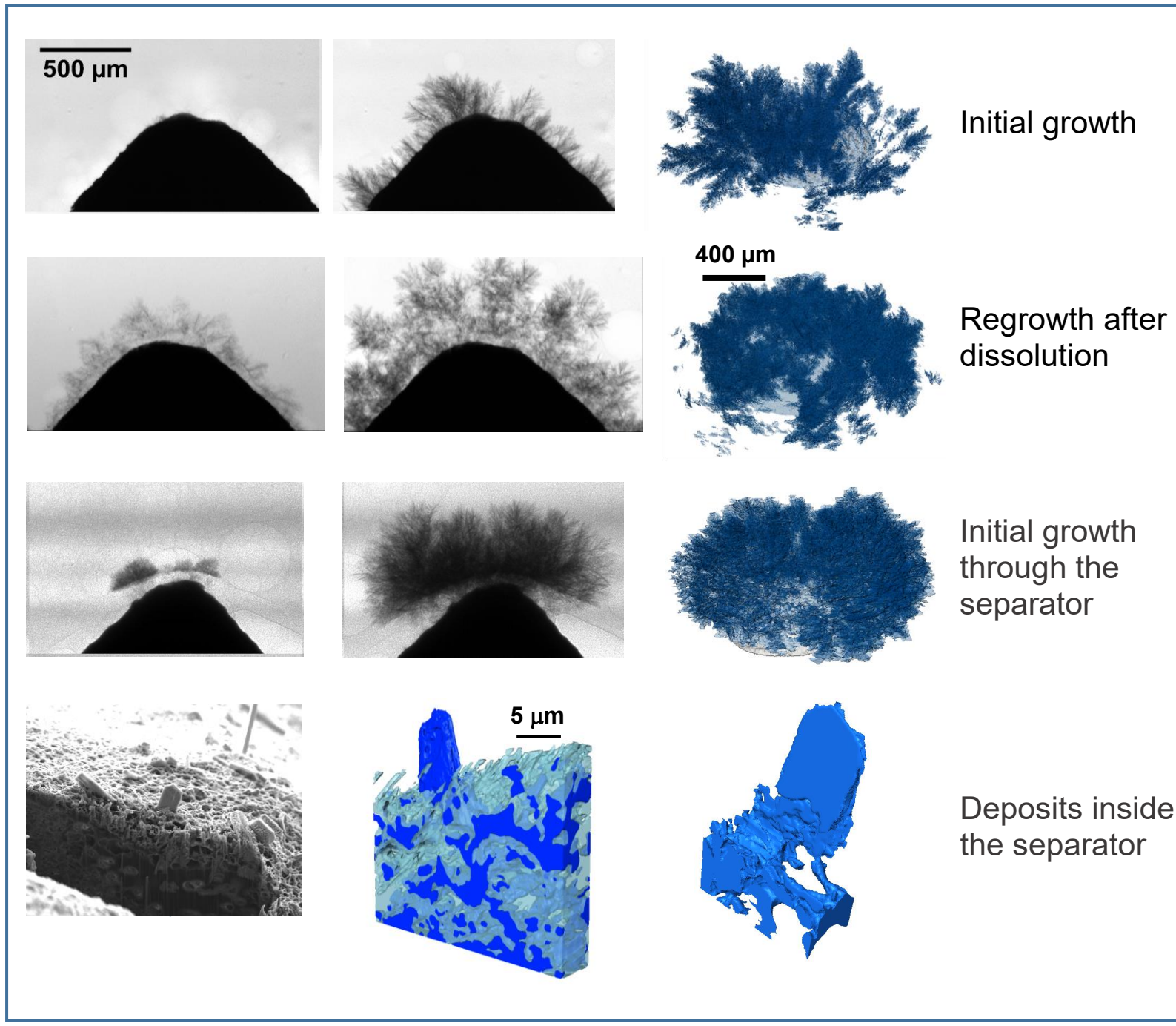

Operando visualisation and multi-scale tomography studies of dendrite formation and dissolution in zinc batteries

Vladimir Yufit[1,*], Farid Tariq[1], David S. Eastwood[2,3], Moshiel Biton[1], Billy Wu[4], Peter D. Lee[3,5] and Nigel P. Brandon[1]

[1] Department of Earth Science and Engineering, Imperial College London, London SW7 2AZ

[2] School of Materials, University of Manchester, Manchester M13 9PL

[3] Research Complex at Harwell, Harwell Oxford, Didcot, Oxfordshire OX11 0FA

[4] Dyson School of Design Engineering, Imperial College London, London SW72AZ

[5] Department of Mechanical Engineering, University College London, London WC1E 6BT

Keywords: battery failure, dendrite formation, synchrotron x-ray tomography, radiography 3D imaging and quantification, FIB-SEM tomography, rechargeable zinc battery,

Summary

Alternative battery technologies are required in order to meet growing energy demands, and address the limitations of present technologies. As such, it is necessary to look beyond lithium ion batteries. Zinc batteries enable high power density while being sources from ubiquitous and cost-effective materials. This paper presents, for the first time known to the authors, multi-length scale tomography studies of failure mechanism in zinc batteries with and without commercial microporous separators. In both cases, dendrites were grown, dissolved and regrown, critically resulting in different morphology of dendritic layer formed on both the electrode and the separator. The growth of dendrites and their volume specific areas were quantified using tomography and radiography data in unprecedented resolution. High-resolution ex-situ analysis was employed to characterise single dendrites, and dendritic deposits inside the separator. The findings provide unique insights into mechanisms of metal-battery failure effected by growing dendrites.

*corresponding author

Introduction

State-of-the-art lithium-ion battery technology is approaching its inherent limitations of maximum energy capacity. As the energy demands of the modern society are constantly increasing, new technologies and approaches are required to develop rechargeable batteries with high capacity. Metal-air batteries represent one class of promising candidates for energy storage applications, with lithium-air batteries promising the highest theoretical specific capacity and energy[1, 2]. Zinc-air batteries are another emerging option, showing a theoretical energy density of 1086 Wh/kg (with oxygen) and low estimated production costs of < 10 $/kWh[3]. However, challenges remain in key areas such as cycle life, reversibility and power density[1, 4]. For example, one of the most common failure mechanisms is caused by metal dendrites that form during the battery charge cycle, and if they grow sufficiently large they may pierce the separator and cause internal short-circuiting and even thermal runaway of the battery.

To alleviate the adverse effects of dendrite growth, it is imperative to gain insights into the mechanisms of dendrite formation through the use of advanced *operando* techniques. This study focuses on the initial growth, dissolution and regrowth of zinc dendrites in alkali zincate electrolyte widely employed for static and flow zinc-air batteries. Nonetheless, the findings of this study can also benefit other metal based systems such as, for example, lithium or sodium-air batteries.

Zinc electrodeposition in alkaline solutions has been studied extensively, and a few correlations have been established between deposit growth rate, electrode surface finishing, total overpotential, zincate concentration and temperature [5-10]. At a given zincate concentration the transition of zinc deposition into dendritic mode was found to be governed by the total overpotential, with higher overpotential values driving the electrochemical reaction into mass-transport limiting mode. Moderate and low values of overpotential significantly affect the morphology of zinc deposits, that may be described as boulder, layered and mossy structures [11-13]. The morphology is also affected by the forced convection of the zincate electrolyte commonly used in zinc-air and zinc-nickel flow batteries [14-16]. These rechargeable zinc-based batteries can operate at quite high current densities[17, 18] well above

50 mA/cm^2. Such high current densities may result in localised dendritic growth that can also be simulated under well-defined boundary conditions[19]. Though this dendritic growth can be mitigated under certain conditions even at high current using different additives[20, 21], it cannot be entirely prevented due to the presence of local inhomogeneities associated with surface roughness of the zinc electrode. As practical rechargeable zin-based batteries usually have quite a large electrodes (> 50 cm^2) there is a high chance for development of local inhomogeneities due to surface roughness (high localised current density), stagnant electrolyte layer (non-uniform flow), limitations of mass transport etc. Such conditions have been re-created in in-situ experiments of the current work in order to demonstrate how dendritic grow can cause irreversible capacity loss, battery degradation and even battery failure.

Prior experimental studies of the electrochemical formation of metal dendrites have been predominantly ***ex-situ***. However, recent advances in scientific instrumentation and electrochemical cell design have enabled some *in-situ* and *operando* studies of dendrite formation by means of confocal laser scanning microscopy, nuclear magnetic resonance spectroscopy, transmission electron and transmission x-ray microscopy [22-25]. Synchrotron and lab-source X-ray computed tomography have been successfully implemented to study the behaviour of zinc anodes and air cathodes in zinc-air batteries during operation [26-28]. However, these prior studies did not capture initial dendrite formation dissolution and successive regrowth with and without the presence of the separator, which is pivotal in providing quantitative evidence for degradation and failure models.

This paper presents an *operando*, temporally resolved investigation of zinc dendrite growth, dissolution and regrowth on bare and separator enclosed zinc electrodes at different length scales by means of synchrotron X-ray computed tomography (SXCT). Regrowth and re-dissolution are critical given that rechargeable cells are expected to run for thousands of charge / discharge cycles.

Although time-resolved tomography is an indispensable method to study the mechanisms of metal dendrite formation in very high temperature systems during the metal solidification, it has only recently been extended to the *operando* study of electrochemical systems[29-31]. SXCT offers the opportunity for non-destructive analytical insight with high spatial and temporal

resolution of two and three-dimensional data of electrode microstructures with a relatively large field of view (typically 1 μm resolution for 5×5×5 mm^3 sample size).

Operando SXCT was performed using a purpose designed cell which replicates the behaviour of a large zinc-air cell in conditions suitable for tomography (supplementary materials, Figure S1). Such an approach can be also adopted to study electrochemically driven dendrite formation, dissolution and separator penetration in other electrochemical systems.

The synchrotron growth/dissolution studies were combined with higher resolution ex-situ FIBSEM to provide true multi-length scale imaging and accurately capture the precise structure of dendrites down to tens of nanometres as they pierce battery membranes leading to a permanent failure. This comparison is vital for a variety of battery systems comprising metal anode such as for example based on organic electrolytes with metallic lithium, sodium or magnesium. Altogether, this methodology provides dynamic and multi-length scale understanding of growth and dissolution mechanisms and the effect of separator on these processes that have never previously been imaged in such detail.

Experimental

Cell assembly

The electrochemical cell used for *operando* synchrotron XCT was constructed inside a Kapton tube of 6 mm interior diameter with a 5 mm zinc rod (Goodfellow) as an anode and a cathode from a dense 5 mm carbon hollow tube (Goodfellow). The zinc anode was machined into a tip of c.a. 200 μm for imaging purposes, and to achieve high local current densities to stimulate dendritic growth. In the first experiment, electrodes were physically separated from each other by a 3 mm gap in separator-less cells. In the second experiment, a microporous hydrophilic polypropylene separator (100 μm thick, VWR) was placed between the zinc tip and the carbon hollow tube. An aqueous electrolyte containing 5M KOH and 0.15M ZnO (Sigma) was added following cell assembly. The cell was cycled under constant current of 10 mA for both deposition and dissolution using an Ivium VERTEX potentiostat, at room temperature and ambient pressure.

Operando experiments and 3D imaging

X-ray imaging of the operating cell was performed at the Diamond Light Source using the Diamond-Manchester imaging beamline I13-2. Monochromatic and polychromatic beams were used to optimise transmission though the sample for first and the second experiments with an effective X-ray detector pixel size of 0.45 and 0.81 μm respectively. Radiography was performed with 0.1-2 s exposures during deposition and dissolution depending on the beam used. 3D tomography imaging was carried out at end of each deposition-dissolution step whilst the cell held at open circuit (OCV) during rotation. Each tomography scan consisted of 1800 projections. 3D volumes were reconstructed from the tomographic data using a filtered backprojection algorithm and visualised with Avizo 9.0 (FEI). The growing dendrites were tracked using in-house algorithm implemented in ImageJ and Matlab.

Ex-situ experiments

Ex-situ analysis of the deposited dendrites was carried out using Zeiss Auriga Cross-beam FIB-SEM. Dendrites grown inside the separators were analysed as-received while those grown on zinc tip were coated in epoxy for structural support. A secondary electron detector was used for the microstructural observation with an acceleration voltage around 1 to 5 kV. A 30 kV Ga ion beam with 2nA current were used to serially section and polish the sample surface while an electron beam captures secondary electron images of the surface. The process was repeated until up to 300 images were captured to provide a full size of dendrites. Image foreshortening and alignment corrections were implemented in using Avizo 9.0 (Thermo Fisher Scientific) to digitally reconstruct 3D data.

Results and Discussion

Zinc dendrite formation, dissolution and regrowth

Zinc electrodeposition in alkaline media is initiated when a negative (reduction) current is applied to the zinc anode according to the half-reaction:

$$Zn(OH)_4^{2-} + 2e^- \rightarrow Zn_{(s)} + 4OH^- \quad , \quad E^0 = -1.199 \text{ V vs SHE} \qquad (1)$$

This reaction, however, is complex and driven via both chemical and electrochemical processes[5, 8]. In the present system zinc dendrites were deposited onto a cone-shaped zinc anode by applying a negative 10 mA current (c.a. 30 mA/cm^2) between zinc anode and carbon

air cathode separated by approximately 3 mm of the aqueous zincate electrolyte. Zinc dendrites do not start to develop until a critical overpotential is reached, which initiates dendrite growth [10]. The time taken to achieve it, is dependent on various parameters such as local current density, concentration, and temperature. Following initiation, Figure 1A shows dendrites, which can be termed small (<c.a. 30 μm) formed on the left part of the tip after 214 s of deposition (see also Figure 1P for the corresponding chronopotentiometric data). These become visible after 100 s under the synchrotron imaging conditions used, indicating the initiation time is < 100 s (video V1). Furthermore it is also seen that zinc dendrite formation is accompanied by a side reaction resulting in hydrogen evolution (visible as white semicircles around the zinc tip) formed via water electroreduction[32]. As zinc deposition proceeds, dendrites appear on various locations on the tip of the cone electrode as well as around it (Figures 1B and 1C after 388 and 561 s of deposition respectively). The different initiation times of various dendrites are likely to be associated with a non-uniform surface finish on the zinc electrode, responsible in turn for non-uniform local current density that affects the critical potential and thus the initiation time. After a period of sufficient deposition (Figures 1D and 1E after 734 and 918 s) secondary dendrites become visible and more dominant. The secondary dendrites grow on the trunk of the primary dendrites rather than directly on the electrode tip itself and prevent primary become any thicker. However, the morphology of both primary and secondary dendrites does not change with main supporting trunks and blade-like branches. This appears to suggest strong dependence on local crystallography and localised current flowing along the secondary dendrites. As before, after a period of growth (Figure 1E) it is possible to see the development of ternary dendrites that are growing from the trunks of secondary dendrites.

The thickness of the primary dendrite has been estimated to be around 2-5 μm and this does not seem to increase further with deposition time. However, the length or height of dendrite trunks and number of branches clearly increase with deposition time, indicative of diffusion controlled growth[11, 13]. The growth of small primary dendrites (longer initiation time) was inhibited by surrounding larger counterparts (>200 μm long) as result of higher surface area of the large dendrites that effectively draw the localised current away from the small dendrites[6]. Moreover, the flow local current is affected by formation of mechanical contacts

between branches of two or more adjacent growing dendrites facilitated by evolving hydrogen bubbles.

The radiography data were used to calculate the estimated growth rate of dendrites at different locations on the tip. Figure 1R presents growth curves of individual dendrites at three locations on the zinc anode tip as schematically indicated by Figure 1Q. Dendrites growing on different locations are characterised by different initiation times. Furthermore, the growth rate at these locations is not homogenous and deviates from the reported linear behaviour[10]. Such deviation points out the change of localised current during dendrite growth, likely associated with the increase of active surface area due to formation of secondary and ternary dendrites as well as with the density and the size of the surrounding primary dendrites. For example, the growth rate of the right-side dendrite located in the less dense area of the tip surrounded by smaller dendrites appears to be linear, as opposed to dendrites in the denser centre and the left side (Figure 1Q). Moreover, the figure confirms that larger primary dendrites have a shorter initiation time.

Through controlling growth, it was possible to acquire 3D synchrotron tomograms of the dendrites; although a few collapsed prior to the start of the experiment. (Figure 1F). Application of a positive 10 mA current for 15 min between the Zn anode and carbon cathode initiates dendrite electro-dissolution or thinning (both branches and trunks) over the electrode surface (Figures 1G). This thinning commences from the topmost parts of the dendrites and propagates down to the tip. Its mechanisms appear to be quite different from the growth where the primary, secondary and ternary dendrites appeared in sequentially one on top of another. As electro-dissolution proceeds, branches of the dendrites become thin enough to collapse on neighbouring dendrites (video V2). This proceeds until dendrite trunks thin to the point where they are no longer attached to the tip resulting in a fallen matted layer of dendrites on the electrode tip (Figure 1H, 447 s of dissolution). Subsequently, the tip itself starts to dissolve and recede (Figures 1I and 1J). Based on comparison of radiographs between start and end of the dissolution (15 min) at different locations, the tip recession distance was estimated to be approximately 60 µm.

The second cycle starts with an application of negative 10 mA current between the partially dissolved tip covered by matted layer of collapsed dendrites formed during the first cycle

(cyc1) and the carbon cathode. As in the first cycle, to the growth of new dendrites (cyc2) on the tip surface accompanied by hydrogen bubble formation was observed in radiography mode. As result, the collapsed and detached cyc1 dendrites were mechanically pushed upwards (Figures 1K and 1L). It was not possible to follow the initial growth of cyc2 dendrites in radiography mode due to their fine features below the resolution (0.45 μm, see experimental section) of the detector and also the presence of cyc2 dendrites surrounding the tip. Eventually, after 1028 s into the second deposition step (Figure 1M) the cyc2 dendrites reconnected with cyc1 ones, resulting in formation of a complex entangled three-dimensional network (Figure 1P). The second cycle is therefore strongly dependent on the surface left from the first cycle, indicating a certain type of a memory effect. As deposition continued, the fallen dendrites provide a mean to form a dense network around the tip as new dendrites formed on the top of this dendrite network (Figure 1R and 1Q). By the end of the second deposition step the Zn anode displays a different morphology with a denser and tortuous region formed around the receded tip, and new dendrites on top of this region. The presence of this denser region effectively impedes the formation of new dendrites on the electrode tip itself. Instead, new dendrites grow from the denser region as result of a decreasing distance between the forming dendrites and the counter-electrode. Essentially, each charge and discharge cycle is modifying a dense Zn metal surface, with porous and tortuous dendrite regions responsible for battery degradation and failure. The effect of repeated cycling (deposition/dissolution) can be observed in video V3 and Figure S3. It is clearly seen that zinc electrode slowly dissolves and recedes and never returns to its initial state during the cycling demonstrating the accelerated degradation of a metal anode in the batteries operating under similar conditions.

In order to compare the morphology of cyc1 and cyc2 dendrites, SXCT scans of the tip of the zinc electrode were carried out at the end of the each electrodeposition step. Figure 2 presents the reconstructed and post-processed 3D visualisation of whole and a specific region of the tip after two successive depositions. As collaborated by Figure 2A (video V4) after the first deposition, the grown dendrites do not cover the whole electrode tip. Moreover, it is clear that the dendrites grow predominantly from microprotrusions around the tip, formed during the machining of the tip. Such a surface roughness is responsible for shorter initiation times in comparison to dendrite growth on smooth surcafes[10]. The dendrites also vary in

thickness and height across the electrode with the highest one located on the top of tip likely due to high value of localised current. The height of largest dendrites varies between 200 - 300 µm, while for small dendrites it is between 50 – 100 µm (Figure 2B).

As also shown by the *operando* x-ray radiography, the resulting structure was influenced at an early stage of growth by different initiation times i.e. the dendrites that formed first remained the largest at the end of the deposition and dominated growth. Moreover, significant number of small dendrites appears around the large ones, resulting in densification of the dendrite base during the first deposition (Figure 2C). 3D tomography confirmed the presence of primary, secondary and ternary dendrites, indicating that the growth in height occurs at a faster rate than densification of their bases resulting in a "spruce-tree" like microstructure, with the trunk and branches protruding from it. Digitally skeletonised dendritic structures (Figure 2D) attest to the densification of dendrites at the base, with an average branch length of 6 µm.

The morphology of the dendrites changed when the dendrites were subjected to dissolution and second deposition or regrowth. Figure 2A indicates that the second deposition resulted in denser dendrite region that still does not completely cover the tip. However it became evident that at the space extending from the tip up to the denser region (c.a. 30 µm) the dendrites were significantly less dense and narrow when compared with their microstructure further away (Figure 2F) and with the first growth (Figure 2C). This is the consequence of several mechanisms. Firstly, as corroborated by the radiography measurements during the dissolution step, dendrites undergo thinning across their whole length. Concurrently, the electrode tip itself recedes. As a result, some dendrites become so thin (below the resolution of X-ray detector) that they eventually collapse leading to the loss of electrical contact. However once deposition is re-initiated, these collapsed dendrites become reattached to the zinc tip and new dendrites start to grow from around old ones. As the deposition proceeds a dense and thick region forms above the electrode surface preventing densification of the electrode tip surface, as occurred in the first deposition step. The skeletonised structure of the dendrites (Figure 2G) reveals that the average branch length remains similar at around 5 µm between the two successive depositions. However, the branches appear substantially more entangled and their number as well as their density and distribution across the zinc electrode is considerably higher after dissolution and re-deposition. This has also been

confirmed by quantification of the surface area and volume of the dendrites based on 3D tomography reconstructed images (Table 1). Accordingly, the total volume and surface area of dendrites is 5.5 and 4.5 times higher between the first and second charge respectively. Moreover, the volume specific area reduced by 17 % after the second charge, indicating that the dendrite network became more compact, most likely in the denser regions as indicated in Figure 2F. This compactification, though does not prevent dendritic growth, may indicate the way to engineer zinc electrodes in order to minimise dendrite formation e.g. through nanostructuring of zinc electrode surface to form a sponge-like electrodes[33].

Effect of current density on Zinc dendrite formation

In order to see the effect of lower current density on zinc dendrite formation, a negative 5 mA current (c.a 15 mA/cm^2) was applied between the zinc anode and carbon air cathode. This value is lower than the calculated limiting current density (20 mA/cm^2) for 0.15 M concentrated solution based on the data provided by Diggle[10] *et al*. The first dendrites became visible in radiography 180 s after the deposition starts, indicating a longer initiation time in comparison to the higher current case (Figure 3A). As zinc deposition continues, dendrites can be seen growing on various locations both on and around the tip (Figure 3B and 3C after 720 s and 860 s respectively). As in the previous cases, the hydrogen bubble formation was accompanying dendritic growth during the entire deposition period (video V5) even at this lower current. The average height of dendrites after 720 and 860 s was 50 and 80 μm respectively. Following 1020 s and 1200 s the dendrites reached an average height of 110 and 150 μm respectively (Figure 3D and 3E), giving an average growth rate of 10 μm/min. This compares with 35 μm/min for the doubling the current indicating a considerably higher growth rate for a higher current. Under these circumstances, the dendrite growth appears to be not purely diffusion limited. Upon finishing electrodeposition, SXCT scan of the tip of the zinc electrode was carried out followed by digital reconstruction of the 3D image of the dendrites depicted by Figure 3F and 3G. As in the higher current case, it is clear that dendrites do not cover entirely cover zinc tip and their growth imitated from microprotrusions around the tip. The dendrites heights vary across the different locations on the tip with largest dendrites being 150 - 200 μm high (Figure 3G). It was also possible to isolate a medium size

single dendrite (c.a. 60 μm) in order to study its internal structure (Figure 3H). Though It is possible to distinguish trunk and secondary dendrites (c.a. 20 μm), the SXCT resolution (0.81 μm) is too low to discern the finer structure of a dendrite that is better resolved using other methods such as FIB-SEM.

The skeletonised structure of the low current dendrites gives the average branch of dendrites 8 μm versus 5 μm for dendrites grown at higher current. Moreover, the high coordination number (number of branches growing from the same joint) for low current dendrites was 6 while for higher current dendrites it was 16. It indicates that lower current dendrites grow higher before branches start forming thus making these dendrites having a thicker trunk (Figure 3H) with less branches. This is also confirmed by calculation of the surface area and volume of the dendrites based on 3D tomography images (Figure 3, table). Subsequently, the volume specific surface area of low current dendrites was 0.63 μm^{-1} as compared against higher current dendrites one of 1.04 μm^{-1}. Such a lower value of volume specific area provides additional indication of dendrite thickening at low current deposition.

In order to investigate the effect of high current density on dendrite formation, a negative c.a. 80 mA/cm^2, was applied between the zinc anode and the counter electrode. The growing dendrite become visible in radiography 71 s after the deposition started, indicating a shortest initiation time in comparison to the low and higher current cases (Supplementary materials, Figure S4 A). As deposition progresses the largest dendrite (number 1) grew to 210, 521 and 821 μm after 143, 222 and 282 s respectively (Figures S4 B-E, video V6). The final dendrite network that formed on the tip of the zinc electrode is depicted in Figure S4 F and can be observed in video V7. In order to find a correlation between observed initiation time (time when the dendrites become visible in radiography) and applied current, the approach suggested by Bai *et al.* has been adopted here[34]. Briefly, a logarithm of initiation time (Sand's time in the cited article) is plotted versus logarithm of current density and the slope of the plot is evaluated via linear fit. Such a plot for zinc dendrites is depicted by Figure S4 H with calculated slope of linear fit being -0.54. This value is lower than that of lithium dendrites in non-aqueous concentrated electrolytes[34] (between -1.18 and -1.42) indicating a significantly faster growth rate of dendrites in the aqueous systems due to considerably higher

conductivity of the electrolyte, lower concentration of zincates and negligible effect of electromigration due to presence of supporting KOH electrolyte.

The growth rate of selected dendrites (Figure S4 G) was evaluated and plotted in Figure S4 I. Clearly, the largest dendrite (designated as dendrite 1) has a highest growth rate that is linear in comparison to smaller dendrites with much lower growth rate that deviates from linear behaviour for in the last 60 s of deposition. Similarly, the number of branches (Figure S4 J) of the largest dendrite was 6 times higher than that of a small dendrite (designated as dendrite 4). This all indicate that the large portion of current is flowing through the large dendrites (similar behaviour was found for a higher current) allowing them to grow and form more branches on expense of the growth of the smaller dendrites. Such a behaviour is extremely detrimental for battery charging at high currents as a single growing dendrite with localised high current density can easily reach the counter electrode within just minutes of operation and permanently short-circuit the battery.

Zinc dendrite formation, dissolution and regrowth: the effect of the porous separator

In order to minimise internal resistance while maintaining proper electrical insulation between the battery anode and cathode an ionically conductive separator (either porous or ion-exchange membrane) is employed. The presence of such an electrically insulating layer adjacent to the electrode will affect the performance of the battery in general, and dendrite formation in particular. In order to investigate the effect of a porous separator on the earlier characterised dendrite growth, similar *operando* experiments were carried out with a microporous membrane separator (0.5 µm mean pore size and 100 µm thickness) between the zinc and carbon electrodes (supplementary materials, Figure S2).

Following the same electrochemical procedure, (see Figure 1F) a negative current of 10 mA was applied between the zinc and carbon electrodes to initiate zinc deposition. As in the previous case the electrodeposition of zinc was accompanied by hydrogen evolution, with some hydrogen bubbles trapped between the separator and the anode. Although it is challenging to view the exact moment of dendritic formation on the tip, nonetheless dendrites become visible as fine structures developing inside the porous separator followed 36 s of deposition. The nature of these finer structures within the membrane below the resolution limit of the synchrotron (0.81 µm) was later captured ex-situ in 3D by high resolution FIBSEM. As deposition proceeded, dendrites continued growing inside for 124 s more before reaching the other side of the separator (Figure 4A and video V8). Once the dendrites broke through the separator they then started to expand and grow on top of it. Though the microporous separator provides a very different media that impedes the dendritic growth (as compared to Figure 1) it cannot prevent its mechanical breakage caused by penetrating dendrites. The presence of the electronically insulating separator alters the local potential distribution inside the separator pores as well as imposing mass transport limitations on the diffusion of zincate and other ions through the tortuous pore network, affecting the growth of dendrites inside. As deposition proceeded a substantial number of dendrites penetrated the separator in multiple locations and continued to grow on the separator surface in different directions (Figure 3B). Evidently, after 430 s (Figure 4C) the surface of the separator became fully covered with the growing dendrites on top of it. Also noteworthy is the densification of dendrites inside the separator. These “interior” dendrites

are attached to the anode tip as well as to the dendrites on top of the separator. This connection is necessary for continued dendritic growth.

In contrast to the previous case without the separator, when dendrites were growing everywhere on the tip (e.g. Figure 1E), dendrites on top of the separator grow both vertically and spread laterally along the separator surface (Figure 4D, 590 s of deposition). Such lateral growth was likely affected by the position, size and shape of the carbon counter electrode (supplementary materials, Figure S2). By the end of the deposition (Figure 4E) the grown dendrites formed a complex dense network of branches connected to the zinc anode tip both on top of and inside the separator, with new finer dendrites growing in all directions.

Application of a subsequent positive 10 mA current between the zinc and carbon electrodes did not initiate immediate zinc dendrite dissolution (video V9). Instead, after 20 s the formation of oxygen bubbles around zinc dendrites was first observed as result of the water oxidation reaction. The dissolution of dendrites was discerned in radiography mode only after 90-120 s (Figure 4F). As zinc dissolution proceeds (after 170 s) the top layer of dendrites began to dissolve. As a result, dendrites became sufficiently thin that they collapsed under their own weight over dendrites beneath them, and also on the separator itself. This is in a manner similar to that outlined earlier (Figures 1F-H). However, after 240 s (Figure 4G) it can been seen that fallen dendrites had accumulated on the separator, forming an electronically conducting and hence short-circuiting path between the anode and the counter electrode. However, this short-circuit was not permanent because, as dissolution continued, part of the electronic path disappeared thus re-enabling the dissolution process for a while before fallen dendrites re-formed the electronic path (see voltage spikes in supplementary materials Figure S5). The rate of dendrite dissolution is significantly reduced since part of the current flowing through the zinc electrode is effectively shunted by the short-circuits. From 680 s to the end of the dissolution step, no significant change in size and denseness of dendrites (Figure 4H) was observed. This indicates that the formation of partial short-circuits becomes a dominant effect, preventing further dissolution of the dendrite network on top of the separator. The radiography data shows that zinc tip itself receded by approximately 11 µm indicating that the dendrite under the separator thinned and detached from the tip thus allowing its continuing dissolution.

An attempt to re-grow partly dissolved dendrites was then carried out by applying a negative 10 mA current for 15 min (video V10). It is apparent that new dendrites started to form during the deposition step, as indicated by densification of the dendrite network on the separator surface and the emergence of new dendrites on the edges of the old ones (Figure 4I, after 304 s). Clearly, the receded tip under the separator has reconnected with the dendrites inside of it to enable dendrite formation on top. However, as a result of the re-growth, the formation of partial short-circuits intensified by reconnecting fallen dendrites located on the separator, impeding the growth of new dendrites. By 656 s of the deposition new large dendrites (c.a. 150 μm) grew on the edges away from the tip between the separator and dendrites network (Figure 4J). No new dendrites formed subsequent to 656 s of the deposition i.e. by this time the zinc-air cell had become completely short-circuited.

As in the previous case of the cell without separator, it was possible to evaluate the dendrite growth with respect to time at different directions on two specific locations around the zinc tip that illustrated by 3D reconstructed XCT tomography image in Figure 4K and video V11. The growth profiles include dendrite formation both in the separator and on top of it. The first dendrites that started to grow inside the separator were located on the left side of the tip. The profile (Figure 4L) indicates that, before the dendrites break out of the separator, their growth slows down after approximately 84 s of the deposition. This may be ascribed to mass transport limitations imposed by the torturous structure of the microporous separator. The growth inside the separator on the right side started later (c.a. 200 s), however the dendrite reached the separator surface faster than those that grew on the left likely to higher local current. Analysis of *operando* radiography data indicates that the dendrites growing on top of the separator have horizontal and vertical components (Figure 4K). Due to resolution limitations (0.81 μm pixel size, see the experimental section) and the high density of the growing dendrites, it was not possible to follow the growth of individual dendrites. Instead the growth rate was estimated based on the expansion of the dendrite “front”. Measured at two different locations on the tip, it is clear that the rate of vertical and horizontal growth is different up to 413 and 326 s for the right and left regions respectively. Thereafter, the rate of vertical and horizontal components of the dendrite growing front on both sides appears to be very similar, though shifted along the X-axis (time) as result of the different initiation times of dendrite growth. The difference between the rate of horizontal and vertical growth arises

as a combined effect of two main factors- the location (distance to zinc tip) and shape of the counter electrode (supplementary materials, Figure S2) and density of dendrites inside the separator During the zinc deposition step the number of dendrites breaking out of the separator is increasing, enabling further growth on the surface of the separator. The change in the growth rate for vertical components may therefore be a result of reaching a certain dendrite density both inside and on top of the separator necessary for higher rate of vertical growth on it (see Figure 3D corresponding to that specific moment). It appears that after approximately 600 s the rate of vertical and horizontal components of dendrite growth become very similar up until the end of the deposition.

Figure 4M presents the reconstructed and post-processed 3D visualisation of the cross section of the zinc tip followed radiography studies. In comparison to Figure 2A there is very little coverage of whole electrode tip with zinc dendrites on the tip itself due to the screening effect of the separator. As shown in Figure 3L, the dendrites first deposit under the separator in the vicinity of the tip where the correct is expected to be higher. These sharp “blade-like” microstructures of the forming dendrites facilitate mechanical perforation of the separator layer. However once inside the separator the morphology of dendrites changes entirely as is discussed in the next section. At the present resolution, it appears highly irregular and is characterised by the presence of regions with quite dense deposits. These zinc deposits promote further dendrite growth on top of the separators, serving as highly electrically conductive current pathways.

The dendrites grown on the top of the separator appear to be substantially denser when compared to those grown on zinc electrode with no separator present (Figure 2). It is confirmed by surface and volume quantification summarised by Table 2. As indicated in the table, the volume and surface area of the dendrites grown on top of the separator are 50 and 8 times larger, respectively when compared to those grown with no separator present. As result the volume specific area of the dendrites on top of the separator is 6.5 times smaller. The skeletonised data reveal also a higher average branch length of ca. 10 µm in comparison to those in Figure 2D. Evidently, most of the densification occurred between 0 and 600 s when the vertical growth rate was lower than that of the horizontal one allowing dendrites to grow thicker (Figure 3L) with significant dendrites branch elongation happening thereafter. Although the presence of a microporous separator cannot stop dendritic growth, it definitely

affects the growth direction. One of the strategies ,therefore, to inhibit it comprises of engineering a separator that will promote the horizontal growth and impede the vertical one, e.g. using a hydrogel based materials[35].

Ex-situ high resolution characterisation of zinc dendrite morphology

SXCT 3D-reconstructed data could not provide insight into finer microstructural details of a single dendrite due to low resolution and contrast between various parts of the dendrites (supplementary materials, Figure S6). Therefore, in order to characterise and accurately capture the high resolution sub-micron structure of the dendrites, *ex-situ* FIB-SEM analysis was carried out. The dendrites that grow under mass transport limitations on zinc electrodes appear like a "forest" of spruce tree-like shapes over the electrode (Figure 5A). Clearly, it is possible to identify a trunk (primary dendrites) and branches (secondary and ternary dendrites) attached to it. However, due to the denseness of the dendrites it was difficult to observe the structure of a single dendrite. For better visualisation of single dendrite structure, an individual dendrite was picked up, isolated from the "forest" and embedded in epoxy for a slice-and-view experiment using FIB-SEM. The meticulous procedure of dendrite extraction, imaging, reconstruction and mechanical simulation in 3D is described in many details elsewhere[36]. As indicated by Figure 5B, the interior of the single dendrite is quite dense and homogenous at the given resolution with some parts found to have a thickness of less than 500 nm. Variations in contrast between parts of the dendrite indicate the different crystalline structure of the branches that grow on the trunk. This is consistent with the observed growth of secondary dendrites from primary dendrites at particular crystallographic surfaces that provide an easier nucleation and growth site[11]. Following the slice-and-view experiment a single dendrite structure was reconstructed in 3D from a stack of generated slices, and is depicted in Figure 5C.

Its trunk is not entirely straight and it starts to bend at c.a. 60 µm from the bottom, likely as result of mechanical pressure exhorted by the growing surrounding dendrites. Although sample preparation cannot be ruled out in bending, the structure of the dendrite is well captured at high resolution. Though the reconstructed dendrite was not the longest one (c.a. 150 µm, compare with Figure 1E) it had the traits shared by most of the deposited dendrites.

The trunk of the dendrite at the bottom of the figure (the part that was attached to zinc electrode) is only 5 μm long with no large branches grown on it up to a height of around 60 μm. Contrastingly, the middle part of the dendrite has branches that extend up to 30 μm. At the top of the dendrite, the length of the branches decreases to c.a. 10 μm. The thickness of the branches varies between 0.5 and 1 μm and it is possible to discern nucleation sites on the branches where ternary dendrites begin to form. Based on FIBSEM 3D data of the single dendrite it is possible to evaluate its volume specific area at the given resolution as presented by Table 3.

It should be pointed out that the difference between the volume specific area of a single dendrite and one calculated for all the dendrites on the tip is only 13% indicating quite a good correlation between SXCT and FIBSEM data. Moreover, based on volume or/and surface area it is possible to estimate the average number of dendrites initially grown on the tip as 320 while for the second growth number of dendrites approaches 1620. This high number of dendrites formed in cycle 2 support the radiography based observation of formation of new dendrites onto of the existing entangled dendrite network with high surface area..

Electron Backscattering Diffraction (EBSD) is a powerful tool to characterise crystalline structures of the metals and could be useful to map crystallographic orientation of the grown dendrites. Zinc electrode with grown dendrites on top of it was embedded in epoxy and polished to get smooth cross-section for EBSD mapping (supplementary materials, Figure S7). Though the mapping of the electrode identified many crystallographic planes, as expected, of polycrystalline zinc, it was not possible to identify and characterise dendrites as as they appear to be too small for detection with some likely to be destroyed during the sample preparation.

It has been already reported that the presence of the separator substantially affects dendrite growth and morphology. Figure 4D demonstrates fracturing of the separator by dendrites growing underneath, with cracks of up to 15 μm width appearing in different locations. It should be noted that the characterisation of dendrites in the separator was carried out at locations away from areas of significant separator damage. A close look into the crack formed in the separator reveals a considerable amount of zinc crystallites beneath the crack, and a few appearing on top of the separator. Some of the crystallites on the top (Figure 5E) looks

like needles, being 800 nm thick and 15 µm long while others appear like boulders being 4 µm wide and 8 µm long. These 'boulder' and 'needle' structures[11, 13] are quite dissimilar to the deposited dendrites and likely formed at much lower local current density, affected by the porous separator and the distance away from the tip of zinc electrode where the most current was concentrated.

Zinc dendrites inside the separator (Figure 5F and G) can be clearly identified from the slice—and-view measurement. The morphology of these dendrites is entirely different from the dendrites growing on top of the separator (Figure 5C), appearing to be a quite dense structures that first progress through filling pores inside the separator. This structure is then attached to 'boulders' and 'needles' on the top of the separator indicating that likely most of the 'boulders' and 'needles' are interconnected between themselves through the underlying dense structure. The growth of this structure is responsible for irreversible damage to the separator through the creation of many deep cracks over the separator surface where the dendrites form. A 3D reconstructed region of the zinc dendrites inside the separator is shown by Figures 5H. The reconstructed image of zinc dendrites indicates that the deposited structure is dense at the given resolution, but tortuous in nature due to the separator. The connection between the dendrite on top of the separator to the deposit inside of it can be seen in Figure 5I. Some of these deposits are more than ten microns long (Figure 5H) indicating that polymer material of the pore walls is removed and 'squeezed' around the deposits as indicated by localised charging effects during SEM analysis (see Figure 5G). Analysis of these deposits and the enclosing separator indicates that the volume specific area of the deposits is only 20% smaller than that of the separator interior (Table 3). In other words deposits fill the pores of the separator that provide preferential diffusion pathways for zincate anions and attain the morphology and shape of the polypropylene (PP) separator pores that is very dissimilar to dendrite formation under limited mass transport. Nonetheless the deposition inside the pores appears to be inhomogeneous with some pores filled with the zinc deposits while the others are not. When the pore that ends on the separator surface becomes filled with zinc deposit it turns into a nucleation site for dendrites to grow on the separator. Once on the separator the dendrites will continue growing and densifying in different directions up until the formation of a permanent short-circuit between a zinc anode and counter electrode.

Conclusions:

Multi-length scale tomography and radiography studies, *operando* and ex-situ, provide unprecedented insight into formation and dissolution of zinc dendrites in alkaline solutions during charge and discharge of metal zinc-air and other zinc based batteries.

It was established that the dendrites start to form on surface inhomogeneities where the local current is high, and proceed to grow to a final state with various length dendrites present on the electrode surface with the longest dendrites having a shortest initiation time. During growth primary, secondary and ternary dendrites form. This growth does not necessary follows the linear behaviour as function of time as it also depends on surrounding dendrites and localised current. Moreover, the higher the operational current density was, the shorter and bigger were the initiation time and the dendrite height respectively. The dissolution process (battery discharge) causes dendrites thinning followed by their collapse, detachment from the electrode surface and thinning of the electrode bulk. Regrowth (battery charge) of the dendrites result firstly in the formation of the new dendrites on the electrode surface followed by their reattachment to the dendrites from the previous cycle, forming a complex entangled network of dendrites with denser regions closer to the electrode tip and new dendrites forming on top of these regions. As result, the total surface and volume of the dendrites between cycles one and two increased by 5.5 and 4.5 times respectively. Once formed the dendrites cannot be completely removed in consecutive cycles by dissolution. Instead, in every following cycle the bulk of the electrode will be covered by an increasingly higher surface area porous metal dendrite network sparsely and inhomogeneously attached to the bulk electrode.

Critically, the presence of the separator significantly affects the growth and morphology of zinc dendrites as described. Dendrites that start growing on the electrode surface eventually penetrate the separator and continue growing inside at different *rate* as they fill the submicron pores of the separator. The morphology of zinc dendrites inside the separator appears as dense and tortuous deposits and is completely different from “spruce-tree” structures growing on zinc electrodes. Dendritic growth is screened through the separator so that the growth direction is not directly in line with the counter-electrode until it has

successfully passed through it. On passing through the separator, dendrites continue growing on top of it both horizontally and vertically covering more of the separator surface. As result, after the growth, dendrites formed a compact entangled network atop with volume specific area 6.5 times less than in the case with no separator present. Following dissolution, topmost part of the dendrites thins and partially detaches with the bulk of dendrites still attached to the separator. The detached dendrites are more mobile than was assumed on the separator and cause temporary short-circuits that becomes permanent during the next deposition step.

Microporous separators widely used in battery systems cannot prevent dendrite formation on the electrode surface and subsequent growth through them. Once the dendrites passed through the separator, it was impossible to dissolve them back entirely and prevent short-circuiting of the system. The findings can serve as a basis to begin understanding metal-battery failure mechanisms as they are affected by dendrite morphology. Consequently, dendrite formation might be mitigated by nano/micro structuring zinc electrode morphology (e.g. using a "spongy" anode) and/or engineering of the separator to enhance the lateral/horizontal component of the dendritic growth in combination with organic and inorganic additives, which effect will be investigated in the future work.

Author contribution

V.Y., F.T., and B.W. initiated this research, designed *operando* cells and carried out electrochemical experiments. D.E. assisted in running synchrotron experiments, reconstructed and processed raw synchrotron data, and generated videos with 3D content. F.T. and V.Y. analysed and quantified the post-processed data. N.P.B., B.W. and P.D.L. participated in discussions and manuscript revisions. M.B. prepared ex-situ samples and carried out FIBSEM and EBSD experiments. V.Y. and F.T. prepared the manuscript with inputs from all other co-authors. All authors have provided their consent to publish the final version of the manuscript.

Acknowledgements

Synchrotron beamtime was awarded by the Diamond-Manchester Collaboration under proposal MT4999. The authors thank Dr Andrew Bodey and Professor Christoph Rau for beamline support and Dr Yuri Merla for helping setting up the experiments. The authors are also grateful for the funding provided by the EPSRC Energy Storage for Low Carbon Grids Project (EP/K002252/1).

References

1. Garcia-Araez, N.; Novak, P., Critical aspects in the development of lithium-air batteries. *J Solid State Electr* **2013,** *17* (7), 1793-1807.
2. Rahman, M. A.; Wang, X. J.; Wen, C. E., High Energy Density Metal-Air Batteries: A Review. *Journal of the Electrochemical Society* **2013,** *160* (10), A1759-A1771.
3. Li, Y.; Dai, H., Recent advances in zinc-air batteries. *Chemical Society reviews* **2014,** *43* (15), 5257-75.
4. Shao, Y. Y.; Ding, F.; Xiao, J.; Zhang, J.; Xu, W.; Park, S.; Zhang, J. G.; Wang, Y.; Liu, J., Making Li-Air Batteries Rechargeable: Material Challenges. *Adv Funct Mater* **2013,** *23* (8), 987-1004.
5. Bockris, J. O.; Nagy, Z.; Damjanovic, A., On the Deposition and Dissolution of Zinc in Alkaline Solutions. *Journal of the Electrochemical Society* **1972,** *119* (3), 285-295.
6. Bockris, J. O.; Nagy, Z.; Drazic, D., On the Morphology of Zinc Electrodeposition from Alkaline Solutions. *Journal of the Electrochemical Society* **1973,** *120* (1), 30-41.
7. Despi, A. R.; Jovanovi, D.; Rakic, T., Kinetics and mechanism of deposition of zinc from zincate in concentrated alkali hydroxide solutions. *Electrochimica Acta* **1976,** *21*, 63-77.
8. Cachet, C.; Saidani, B.; Wiart, R., The behavior of zinc electrode in alkaline electrolytes .1. A kinetic-analysis of cathodic deposition. *Journal of the Electrochemical Society* **1991,** *138* (3), 678-687.
9. Cachet, C.; Saidani, B.; Wiart, R., The behavior of zinc electrode in alkaline electrolytes II. A kinetic analysis of anodic dissolution. *Journal of the Electrochemical Society* **1992,** *139* (3), 644-654.
10. Diggle, J. W.; Despic, A. R.; Bockris, J. O., The Mechanism of the Dendritic Electrocrystallization of Zinc. *Journal of the Electrochemical Society* **1969,** *116* (11), 1503-1514.
11. Diggle, J. W.; Fredericks, R. J.; Reimschuessel, A. C., Crystallographic and morphological studies of electrolytic zinc dendrites grown from alkaline zincate solutions. *Journal of Materials Science* **1973,** *8*.
12. Moshtev, R. V.; Zlatilova, P., Kinetics of growth of zinc dendrite precursors in zincate solutions. *Journal of Applied Electrochemistry* **1978,** *8*, 213-222.
13. Wang, R. Y.; Kirk, D. W.; Zhang, G. X., Effects of Deposition Conditions on the Morphology of Zinc Deposits from Alkaline Zincate Solutions. *Journal of The Electrochemical Society* **2006,** *153* (5), C357.
14. Zhang, L.; Cheng, J.; Yang, Y.-s.; Wen, Y.-h.; Wang, X.-d.; Cao, G.-p., Study of zinc electrodes for single flow zinc/nickel battery application. *Journal of Power Sources* **2008,** *179* (1), 381-387.
15. Ito, Y.; Wei, X.; Desai, D.; Steingart, D.; Banerjee, S., An indicator of zinc morphology transition in flowing alkaline electrolyte. *Journal of Power Sources* **2012,** *211*, 119-128.
16. Desai, D.; Wei, X.; Steingart, D. A.; Banerjee, S., Electrodeposition of preferentially oriented zinc for flow-assisted alkaline batteries. *Journal of Power Sources* **2014,** *256*, 145-152.
17. Cheng, Y.; Xi, X.; Li, D.; Li, X.; Lai, Q.; Zhang, H., Performance and potential problems of high power density zinc–nickel single flow batteries. *RSC Advances* **2015,** *5* (3), 1772-1776.
18. Bockelmann, M.; Kunz, U.; Turek, T., Electrically rechargeable zinc-oxygen flow battery with high power density. *Electrochemistry Communications* **2016,** *69*, 24-27.
19. Wang, K.; Pei, P.; Ma, Z.; Chen, H.; Xu, H.; Chen, D.; Wang, X., Dendrite growth in the recharging process of zinc–air batteries. *Journal of Materials Chemistry A* **2015,** *3* (45), 22648-22655.
20. Xu, M.; Ivey, D. G.; Qu, W.; Xie, Z., Study of the mechanism for electrodeposition of dendrite-free zinc in an alkaline electrolyte modified with 1-ethyl-3-methylimidazolium dicyanamide. *Journal of Power Sources* **2015,** *274*, 1249-1253.
21. Gallaway, J. W.; Gaikwad, A. M.; Hertzberg, B.; Erdonmez, C. K.; Chen-Wiegart, Y.-c. K.; Sviridov, L. A.; Evans-Lutterodt, K.; Wang, J.; Banerjee, S.; Steingart, D. A., An In Situ Synchrotron Study of Zinc Anode Planarization by a Bismuth Additive. *Journal of The Electrochemical Society* **2014,** *161* (3), A275-A284.

22. Bhattacharyya, R.; Key, B.; Chen, H.; Best, A. S.; Hollenkamp, A. F.; Grey, C. P., In situ NMR observation of the formation of metallic lithium microstructures in lithium batteries. *Nat Mater* **2010,** *9* (6), 504-510.
23. Nishikawa, K.; Mori, T.; Nishida, T.; Fukunaka, Y.; Rosso, M.; Homma, T., In Situ Observation of Dendrite Growth of Electrodeposited Li Metal. *Journal of the Electrochemical Society* **2010,** *157* (11), A1212-A1217.
24. White, E. R.; Singer, S. B.; Augustyn, V.; Hubbard, W. A.; Mecklenburg, M.; Dunn, B.; Regan, B. C., In Situ Transmission Electron Microscopy of Lead Dendrites and Lead Ions in Aqueous Solution. *Acs Nano* **2012,** *6* (7), 6308-6317.
25. Gallaway, J. W.; Gaikwad, A. M.; Hertzberg, B.; Erdonmez, C. K.; Chen-Wiegart, Y. c. K.; Sviridov, L. A.; Evans-Lutterodt, K.; Wang, J.; Banerjee, S.; Steingart, D. A., An In Situ Synchrotron Study of Zinc Anode Planarization by a Bismuth Additive. *Journal of the Electrochemical Society* **2013,** *161* (3), A275-A284.
26. Arlt, T.; Schroder, D.; Krewer, U.; Manke, I., In operando monitoring of the state of charge and species distribution in zinc air batteries using X-ray tomography and model-based simulations. *Physical chemistry chemical physics : PCCP* **2014,** *16* (40), 22273-80.
27. Schröder, D.; Arlt, T.; Krewer, U.; Manke, I., Analyzing transport paths in the air electrode of a zinc air battery using X-ray tomography. *Electrochemistry Communications* **2014,** *40*, 88-91.
28. Haibel, A.; Manke, I.; Melzer, A.; Banhart, J., In Situ Microtomographic Monitoring of Discharging Processes in Alkaline Cells. *Journal of The Electrochemical Society* **2010,** *157* (4), A387.
29. Kareh, K. M.; Lee, P. D.; Atwood, R. C.; Connolley, T.; Gourlay, C. M., Revealing the micromechanisms behind semi-solid metal deformation with time-resolved X-ray tomography. *Nat Commun* **2014,** *5*.
30. Cai, B.; Karagadde, S.; Rowley, D.; Marrow, T. J.; Connolley, T.; Lee, P. D., Time-resolved synchrotron tomographic quantification of deformation-induced flow in a semi-solid equiaxed dendritic Al–Cu alloy. *Scripta Materialia* **2015,** *103*, 69-72.
31. Tariq, F.; Yufit, V.; Eastwood, D. S.; Merla, Y.; Biton, M.; Wu, B.; Chen, Z.; Freedman, K.; Offer, G.; Peled, E., In-Operando X-ray Tomography Study of Lithiation Induced Delamination of Si Based Anodes for Lithium-Ion Batteries. *Ecs Electrochem Lett* **2014,** *3* (7), A76-A78.
32. Hsu, P. C.; Seol, S. K.; Lo, T. N.; Liu, C. J.; Wang, C. L.; Lin, C. S.; Hwu, Y.; Chen, C. H.; Chang, L. W.; Je, J. H.; Margaritondo, G., Hydrogen bubbles and the growth morphology of ramified zinc by electrodeposition. *Journal of the Electrochemical Society* **2008,** *155* (5), D400-D407.
33. Parker, J. F.; Chervin, C. N.; Nelson, E. S.; Rolison, D. R.; Long, J. W., Wiring zinc in three dimensions re-writes battery performance-dendrite-free cycling. *Energy & Environmental Science* **2014,** *7* (3), 1117-1124.
34. Bai, P.; Li, J.; Brushett, F. R.; Bazant, M. Z., Transition of lithium growth mechanisms in liquid electrolytes. *Energy & Environmental Science* **2016,** *9* (10), 3221-3229.
35. Saito, M.; Nishimura, T.; Yanagida, D.; Satoh, S.; Nishiumi, K.; Akuta, R.; Okamoto, K., Suppression of Dendrite Formation by Using a Hydrogel Separator for Zinc Alkaline Battery. *Electrochemistry* **2017,** *85* (10), 637-639.
36. Biton, M.; Tariq, F.; Yufit, V.; Chen, Z.; Brandon, N., Integrating multi-length scale high resolution 3D imaging and modelling in the characterisation and identification of mechanical failure sites in electrochemical dendrites. *Acta Materialia* **2017,** *141* (Supplement C), 39-46.

Figure 1. Operando study of zinc dendrite growth, dissolution and regrowth in the cell without separator at current density of 30 mA/cm^2.

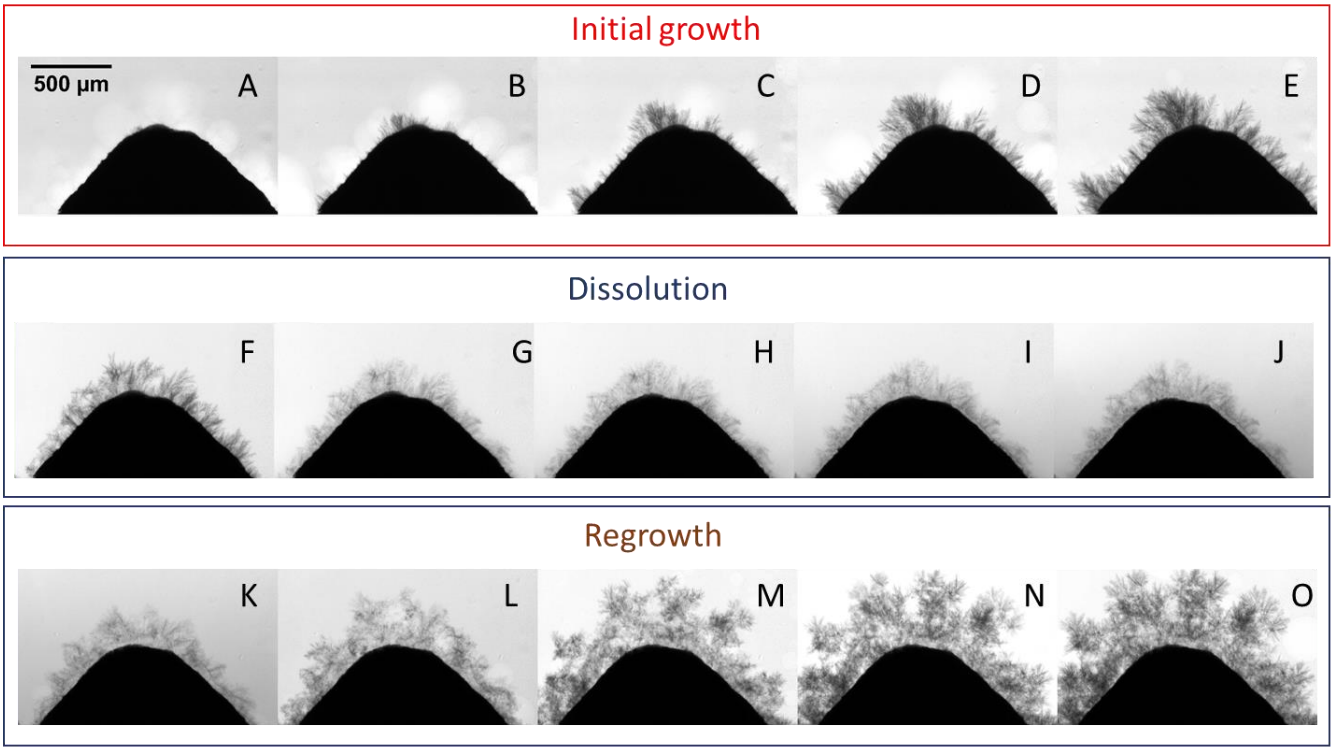

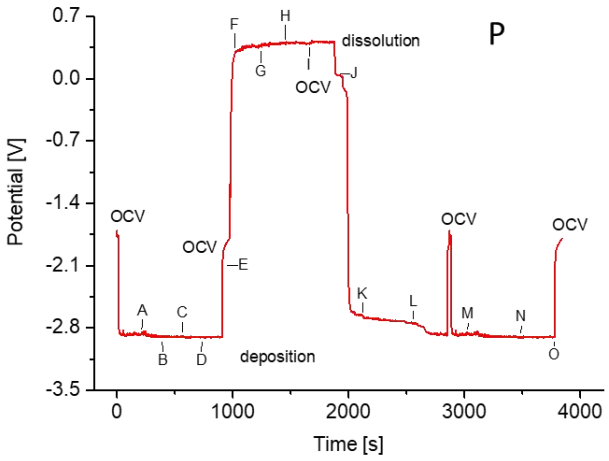

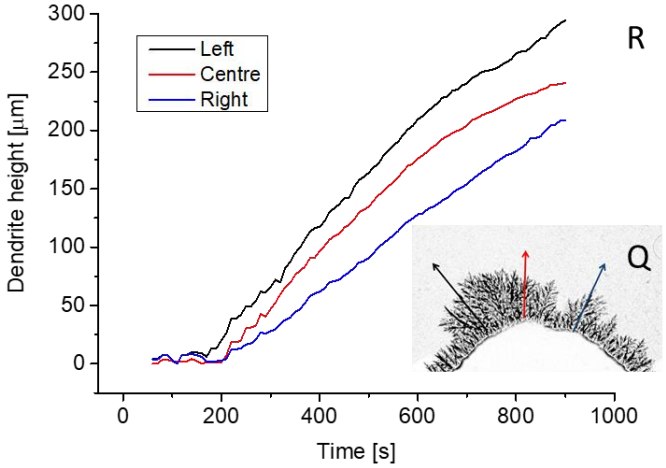

Zinc dendrite growth after A) 214 s, B) 388 s, C) 561 s, D) 734 s and E) 918 s. Zinc dendrite dissolution after F) 10 s, G) 229 s, H) 447 s, I) 655 s and J) 873 s. Zinc dendrite regrowth after K) 122 s, L) 589 s, M) 1028 s, N) 1485 s and O) 1953 s. Chronopotentiometric curve of zinc deposition and dissolution corresponding to the radiography experiments P). Dendrite height/length versus time at certain locations on the tip R) and Q) three locations for direct probing of dendrite growth.

Figure 2. 3D analysis of zinc dendrites.

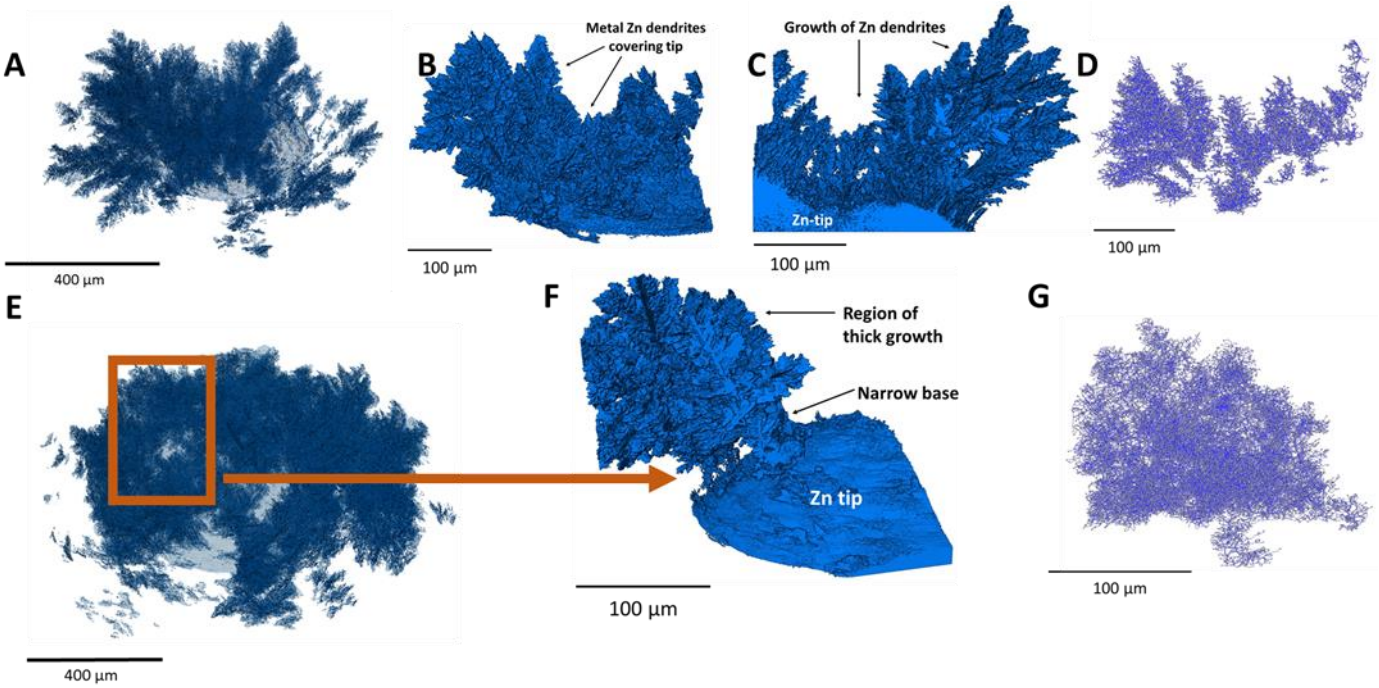

A-C) reconstructed 3D image of dendrites on zinc anode tip following the initial growth, D) skeletonised image of the dendrites, E) 3D reconstruction of the tip with regrown dendrites, F) reconstructed 3D image of the regrown dendrite cluster G) skeletonised image of the regrown dendrites on the zinc anode tip.

.

Figure 3. Operando study of zinc dendrite growth at 15 mA/cm^2 in the cell without separator.

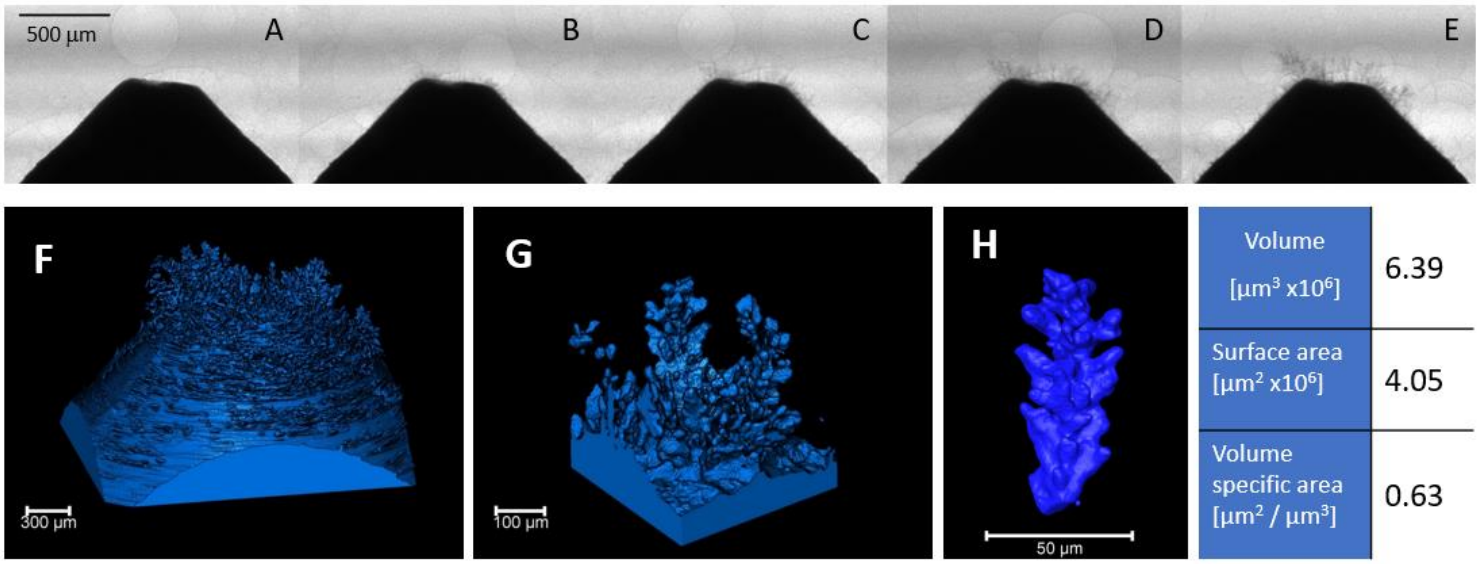

Volume [µm^3 x10^6]	6.39
Surface area [µm^2 x10^6]	4.05
Volume specific area [µm^2 / µm^3]	0.63

Zinc dendrite growth after A) 180 s, B) 720 s, C) 860 s, D) 1020 s and E) 1200 s. 3D analysis of zinc dendrites: F) 3D reconstructed tip, G) 3D reconstructed image of dendritic cluster, H) 3D reconstructed single dendrite. Table with dendrite volume, surface and volume specific surface.

Figure 4. Operando study of zinc dendrite growth, dissolution and regrowth at 30 mA/cm^2 in the cell with the porous separator.

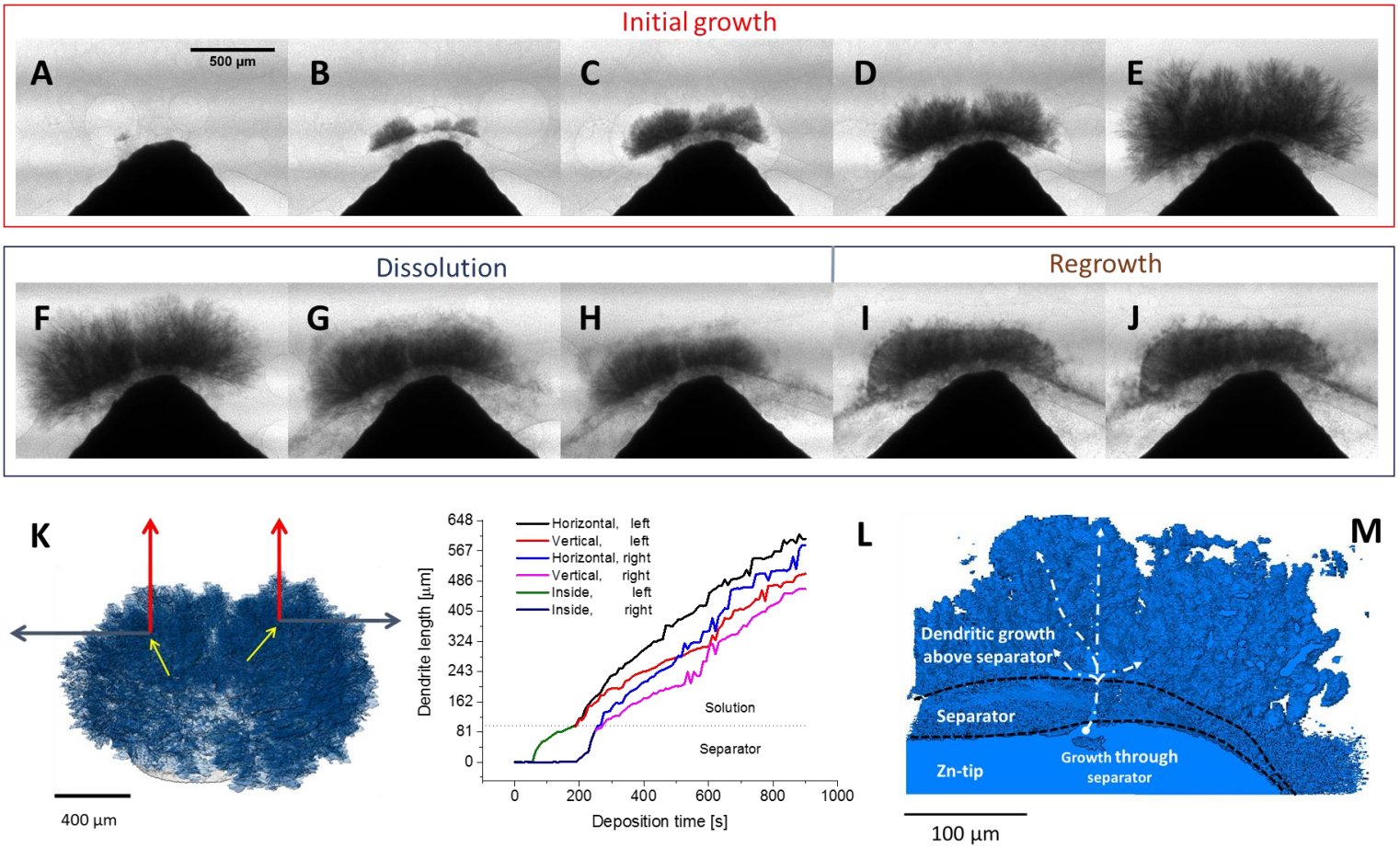

Zinc dendrite growth after A) 200 s, B) 300 s, C) 430 s, D) 590 s and E) 890 s. Zinc dendrite dissolution after F) 120 s, G) 240 s and H) 680 s. Zinc dendrite regrowth after I) 304 s and J) 656 s. K) Reconstructed 3D image of the dendrites and the on top of the separator and the tip indicating dendrite growth directions. L) Dendrite growth vs. time on left and right sides of the zinc anode. M) Cross-sectional image of the dendrites that have perforated the separator after the initial growth.

Figure 5. FIB-SEM analysis of zinc dendrites grown at 30 mA/cm^2.

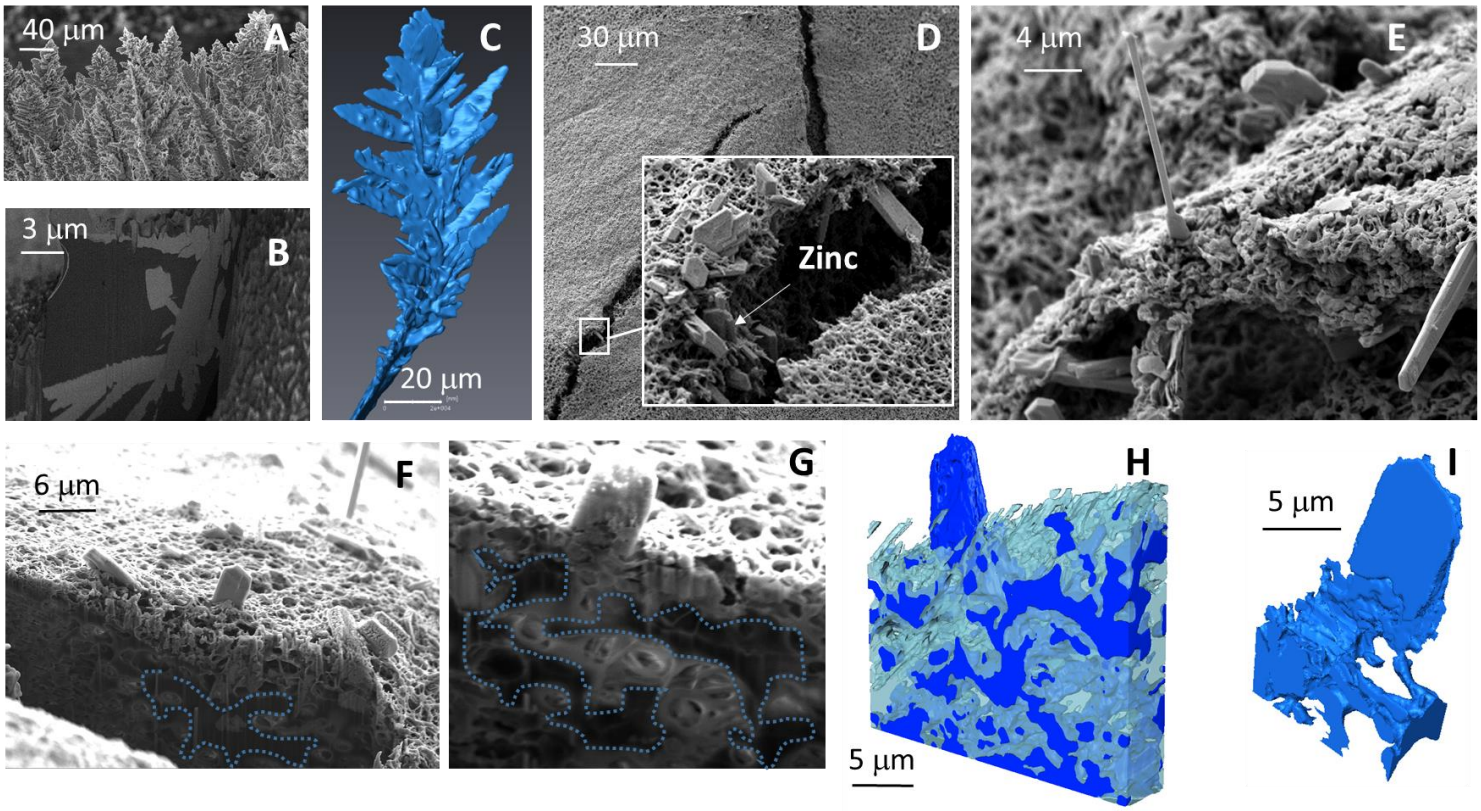

A) Deposited dendrites B) Cross sectional view of a single dendrite embedded in epoxy. C) 3D reconstructed image of the single dendrite, FIB-SEM micrographs of D) Separator torn by dendrites E) Fine dendrite structures grown through the separator F) Cross-sectional view of the dendrites grown inside the separator G) Cross-sectional view of zinc deposits in the separator outlined by dotted lines that are connected to the dendrites on top of it. H) and I) 3D reconstructed image of the zinc dendrite that is attached to the zinc deposits (dark blue) grown inside the porous separator (transparent light blue).

Tables.

Table 1. Surface area and volume of the dendrites after first and second growth

	Volume [μm^3 x10^6]	Surface area [μm^2 x10^6]	Volume specific area [μm^2 / μm^3]
First growth	6.01	6.24	1.04
Second growth	33.0	28.3	0.86

Table 2. Surface area and volume of the dendrites with and without separator after initial growth

	Voxel resolution [µm]	Volume [μm^3 x10^6]	Surface area [μm^2 x10^6]	Volume specific area [μm^2 / μm^3]
No separator	0.45	6.01	6.24	1.04
With separator	0.81	312.76	50.16	0.16

Table 3. Surface area and volume of dendrites on and inside the separator after initial growth

	Voxel resolution [µm]	Volume [μm^3]	Surface area [μm^2]	Volume specific area [μm^2 / μm^3]
Dendrites on tip	0.45 (XMT)	6.01 x10^6	6.24 x10^6	1.04
Single dendrite	0.39 (FIBSEM)	0.0175 x10^6	0.0209 x10^6	1.19
Inside the separator				
Dendrites (Zn)	0.04 (FIBSEM)	0.89 x10^3	2.43 x10^3	2.7
Separator (PP)	0.04 (FIBSEM)	1.25 x10^3	3.88 x10^3	3.1

Supplementary materials.

In order to carry out in-operando SXCT experiments conditions, a special tubular cell have been designed and assembled, as indicated by Figure S1. One end of the zinc electrode was machined into a conical shape in order to minimise X-rays attenuation by bulk of the zinc electrode and allowing study of dendritic growth at submicron resolution.

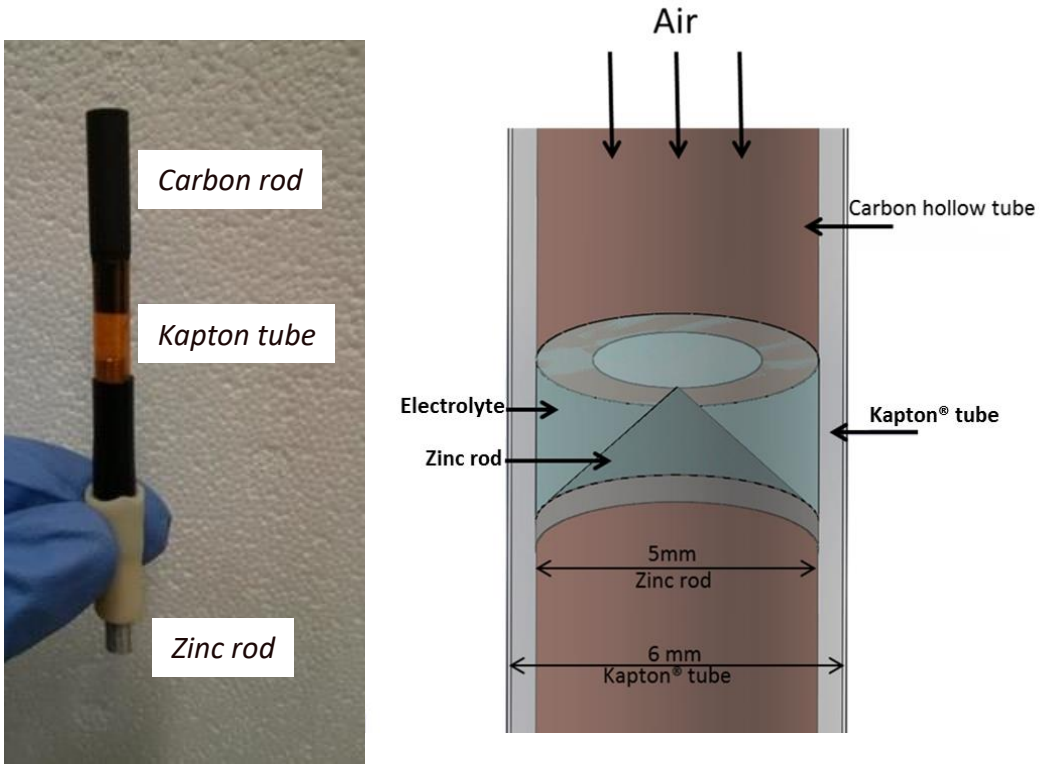

Figure S1. Operando cell used in synchrotron tomography experiments and its CAD design

For *operando* experiments involving microporous separators, they were sandwiched between conical zinc anode and hollow carbon tube electrode as indicated by 3D CAD visualisation in Figure S2.

Figure S2. CAD rendering of the cross-sectional part of the in-operando cell showing the location of separator, carbon and zinc electrodes

Successive steps of equal time length for dendrite formation and dissolution corresponding to charge and discharge in a battery indicate irreversible erosion of bulk of the zinc electrode. Initial electrodeposition (Figures S3 A-B) produced sharp, sword-like dendrites that partially dissolved upon the completion of the first dissolution step (Figure S3 C). Second and subsequent deposition-dissolution cycles resulted in a mixture of fresh, sharp dendrites on the top of the thickened mossy structures (Figures S3 D-E). By the end of the 5th cycle, the bulk of zinc electrode receded by c.a. 100 μm causing significant detachment of large dendrite agglomerates that are floating around mossy regions located the zinc tip (Figure S3 F).

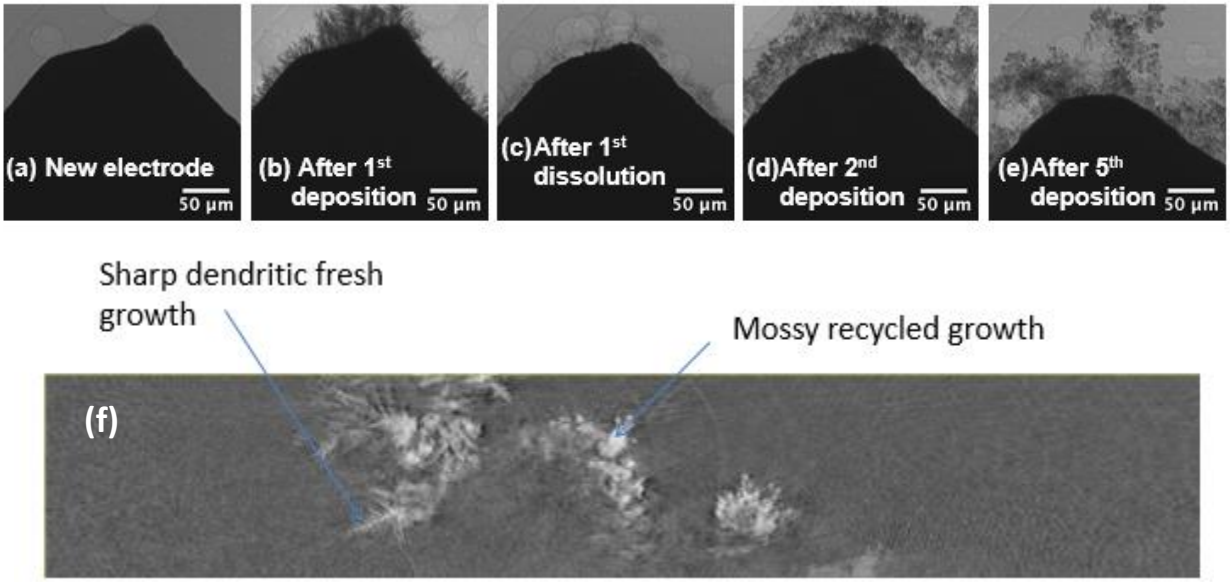

Figure S3. Time sequence radiography showing the irreversibility of the growth process under repeated deposition and dissolution cycles. (a) fresh zinc electrode, (b) initial dendritic growth, (c) first dissolution of the dendrites, (d) zinc electrode after two deposition-dissolution cycles, (e)zinc electrode after 5 deposition-dissolution cycles and (f) cross-sectional view of zinc tip at the end of the cycling

Dendritic growth under a very high current density of c.a. 80 mA/cm^2 was carried out in zinc-zinc cell where one zinc electrode was dissolving and dendrites were growing on another one. Zinc electrodes were 2 mm diameter rods, sourced from Goodfellow. During a very short time of the deposition (< 5 min), some of the dendrites reached a height of almost 1 mm. These and other dendrites were quantified in 2D to estimate their height and approximate number of branches. 2D dendrites were skeletonised and their number of branches were determined using AVIZO 9.0 software. Accordingly, the large dendrites have a higher growth rate and more branches as they grow. The initiation times under different current densities are compared as well in the logarithmic plot.

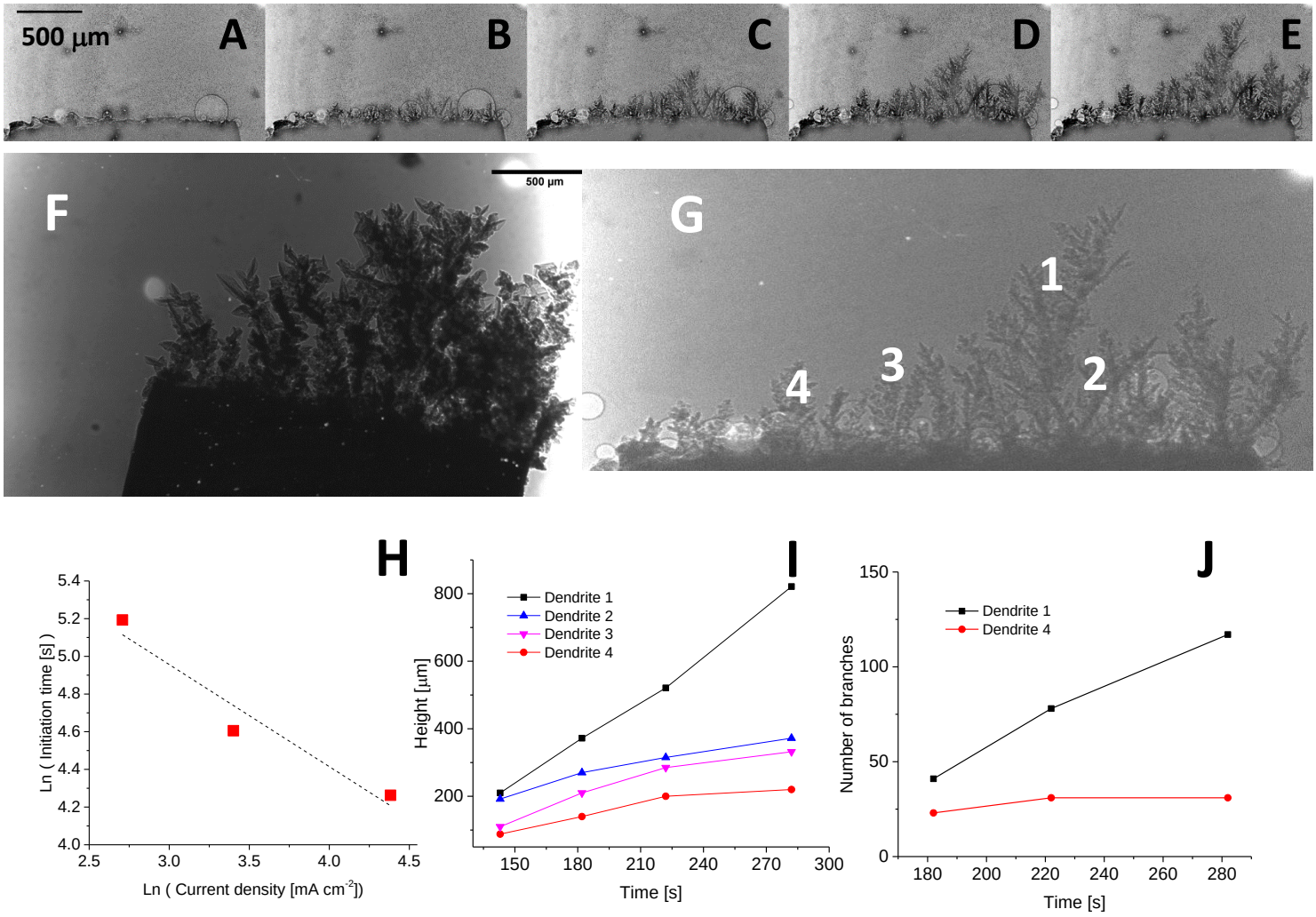

Figure S4. Time sequence radiography of dendrites growing under high current density of 80 mA/cm^2.after A) 71 s, B) 143 s, C) 182 s, D) 222 s, E) 282 s. F) radiograph of fully grown dendrites, G) dendrite selection for analysis H) Logarithmic plot of dendrite initiation time vs corresponding current density with linear fit I) Selected dendrite growth rate and J) Estimated number of branches for selected dendrites

During initial dendrite formation in the in-operando cell with a separator, no voltage spikes were observed indicating that the growing dendrites have not short-circuited the cell. However, during the dissolution step a first voltage spike was observed after 5 min since the dissolution started strongly suggesting the formation of a temporal short-circuit. It disappeared shortly after and the dissolution continued. During the re-growth (second deposition) the permanent short-circuit occurred thus stopping any further cell operation.

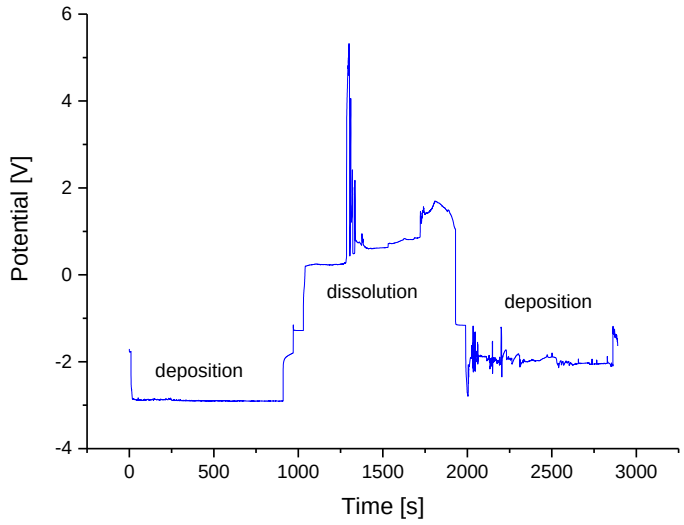

Figure S5. Chronopotentiometric experiments in in-operando cell with a microporous separator. Voltage spikes associated with a short-circuit formation are distinguished during dissolution and re-growth steps.

A single dendrite was identified and 3D-reconstructed using synchrotron data. As indicated in Figure S6 it is possible to discern secondary dendrites (branches) attached to the primary dendrite (trunk). However, low resolution of the detector (800 nm) and contrast does not allow getting a closer look into finer structure of a single dendrite, neither it is possible to isolate a single dendrite from the dendrite agglomerates thus requirng the use of other thecniques such as FIBSEM.

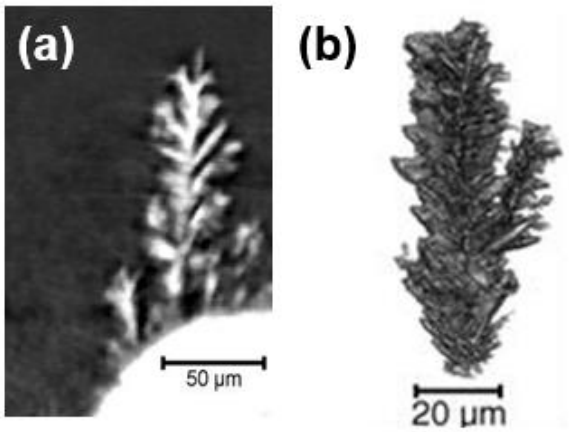

Figure S6. (a) Cross-sectional and (b) 3D reconstructed dendrite structure from a synchrotron tomography experiment at resolution of 800 nm

Zinc electrode with deposited dendrites was embedded into epoxy and carefully polished to exposed a cross section with connected dendrites. This cross-section with regions of connectivity between the dendrites and zinc electrode has been investigated using EBSD (electron back-scattering diffraction). A crystal orientation map of the edge of the tip is clearly seen and pointing out polycrystalline structure of the zinc electrode. However, the dendrites could not be clearly seen in the EBSD map; moreover it is difficult to find a trend between crystallographic orientation of the grains and the dendrites, nor to examine if a preferred dendrite growth orientation is present. More robust and methods of sample preparation with a great deal of precision are required and can be explored in the future work.

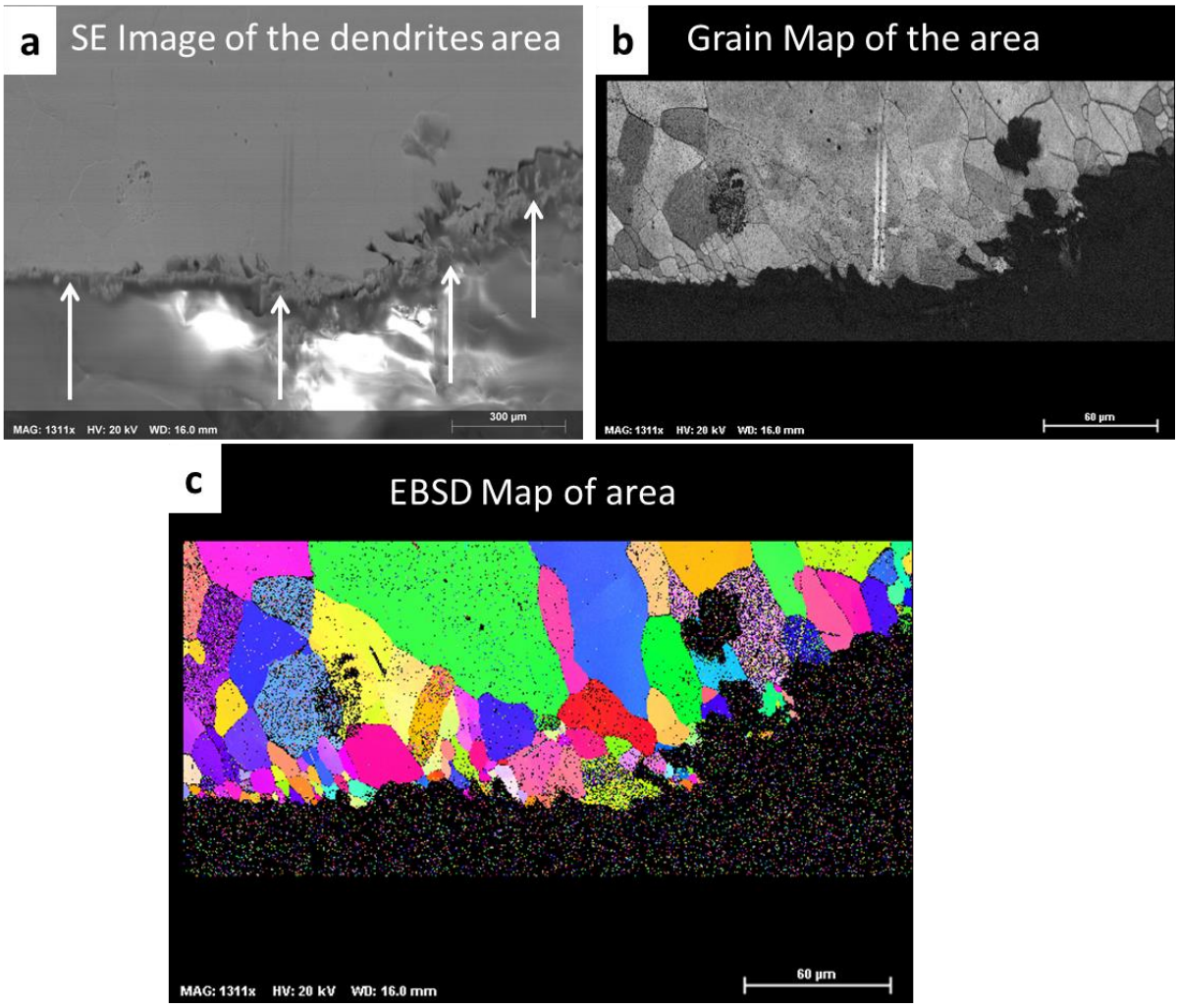

Figure S7. EBSD inspection of the dendrites area connected to the dense tip; (a) SE SEM image of the same area, (b) a grain map of the area and (c) EBSD map of the area.

Click here to access/download

Supplemental Videos and Spreadsheets

video V1 (zn_dendrites_inital_growth).avi

Click here to access/download

Supplemental Videos and Spreadsheets

video V2 (zn_dendrites_dissolution_regrowth).avi

Click here to access/download

Supplemental Videos and Spreadsheets

video V3 (zn_electrode_dissolution).avi

Click here to access/download

Supplemental Videos and Spreadsheets

video V4 (zn_dendrites_in_3D).avi

Click here to access/download

Supplemental Videos and Spreadsheets

video V5 (zn_dendrites_growth_lowcurrent).avi

Click here to access/download

Supplemental Videos and Spreadsheets

video V6 (zn_dendrites_growth_highcurrent).avi

Click here to access/download

Supplemental Videos and Spreadsheets

video V7 (zn_dendrites_highcurrent_aftergrowth).avi

Click here to access/download

Supplemental Videos and Spreadsheets

video V8 (zn_dendrites_initial_growth_on_separator).avi

Click here to access/download

Supplemental Videos and Spreadsheets

video V9 (zn_dendrites_dissolution_on_separator).avi

Click here to access/download

Supplemental Videos and Spreadsheets

video V10 (zn_dendrites_regrowth_on_separator).avi

Click here to access/download

Supplemental Videos and Spreadsheets

video V11 (zn_dendrites_on_separator_in_3D).avi